



## Article

# Integration of Vertical and Horizontal Deformation Derived by SAR Observation for Identifying Landslide Motion Patterns in a Basaltic Weathered Crust Region of Guizhou, China

Yifei Zhu <sup>1,2,3,4</sup> , Xin Yao <sup>1,2,3,\*</sup>, Chuangchuang Yao <sup>1,2,3</sup>, Zhenkai Zhou <sup>1,2,3,4</sup>, Zhenkui Gu <sup>1,2,3</sup> and Leihua Yao <sup>4</sup><sup>1</sup> Key Laboratory of Active Tectonics and Geological Safety, Ministry of Natural Resources, Beijing 100081, China<sup>2</sup> Research Center of Neotectonism and Crustal Stability, China Geological Survey, Beijing 100081, China<sup>3</sup> Institute of Geomechanics, Chinese Academy of Geological Sciences, Beijing 100081, China<sup>4</sup> School of Engineering and Technology, China University of Geosciences (Beijing), Beijing 100083, China

\* Correspondence: yaoxin@mail.cgs.gov.cn

**Abstract:** In recent years, due to adverse geological conditions, intense human engineering activities, and extreme weather conditions, catastrophic landslides have frequently occurred in southwest China, causing severe loss of life and property. Identifying the kinematic features of potential landslides can effectively support landslide hazard prevention. This study proposes a remote sensing identification method for rotational, planar traction, and planar thrust slides based on geomorphic features as well as vertical and slope-oriented deformation rates. Rotational landslides are characterized by similar vertical and horizontal deformation rates, with vertical deformation mainly occurring at the head and gradually decreasing along the slope, while horizontal deformation mainly occurs at the foot and gradually increases along the slope. As for the planar slide, the dominant deformation is in the horizontal direction. It is further classified into the planar traction and planar thrust types according to the driving position. The vertical deformation of planar traction slides is concentrated at the foot, while the vertical deformation of planar thrust slides is concentrated at the head of the landslide. We identified 1 rotational landslide, 10 planar traction landslides and 10 planar thrust landslides in the basalt weathering crust area of Guizhou. Field investigations of three landslides verified the method's accuracy. Combining two-dimensional rainfall and time-series deformations, we found that there is a significant positive correlation between landslide deformation acceleration and precipitation. The landslide kinematic identification method proposed in this paper overcomes the shortcomings of the inability to accurately characterize landslide motion by line-of-sight displacement and realizes the non-contact identification of active landslide motion patterns, which is an essential reference value for geological disaster prevention and control in the study area.



**Citation:** Zhu, Y.; Yao, X.; Yao, C.; Zhou, Z.; Gu, Z.; Yao, L. Integration of Vertical and Horizontal Deformation Derived by SAR Observation for Identifying Landslide Motion Patterns in a Basaltic Weathered Crust Region of Guizhou, China. *Remote Sens.* **2022**, *14*, 4014. <https://doi.org/10.3390/rs14164014>

Academic Editors: Yi Wang, Jun Hu and Weile Li

Received: 6 July 2022

Accepted: 16 August 2022

Published: 18 August 2022

**Publisher's Note:** MDPI stays neutral with regard to jurisdictional claims in published maps and institutional affiliations.



**Copyright:** © 2022 by the authors. Licensee MDPI, Basel, Switzerland. This article is an open access article distributed under the terms and conditions of the Creative Commons Attribution (CC BY) license (<https://creativecommons.org/licenses/by/4.0/>).

**Keywords:** InSAR observation; two-dimensional displacement; landslide motion pattern; weathered basalt; Guizhou

## 1. Introduction

The scale and deformation pattern are two key factors affecting the magnitude of landslide risk, so the identification of landslide boundaries and kinematic characteristics are the two main tasks of landslide hazard prevention and control. The traditional geological engineering survey obtains landslide boundaries and deformation patterns by deformation phenomena and structural characteristics of geotechnical bodies, which is expensive and inefficient. The optical remote sensing method extracts static deformation information of landslides in the development and destruction stages to determine the boundary and scale. However, it is difficult to quantitatively evaluate the kinematic characteristics of landslides [1–3]. As an active microwave remote sensing technique, differential synthetic aperture radar interferometry (D-InSAR) can quickly and efficiently obtain surface deformation by calculating the phase difference of echoes at different times in the same area [4,5].

Thanks to its microwave measurement method, it overcomes the problems of optical remote sensing methods in satellite Earth observation, which are obscured by weather and clouds. In addition, compared with the in situ monitoring technology, the surface deformation characteristics obtained by InSAR can reflect the overall deformation pattern of slopes more completely [6–8]. With the data-processing methods such as Stacking-InSAR, SBAS-InSAR and PS-InSAR being proposed [9–11], InSAR technology has gradually become an essential tool for active landslide identification and kinematic analysis.

Researchers have made much progress in active landslide location identification [12–14], boundary delineation [15–17] and displacement monitoring [18–20] using the line-of-sight (LOS) deformation obtained by InSAR. However, the research on landslide mechanism analysis by integrating InSAR displacement information and geomorphological features is insufficient. With the powerful ground observation capability of InSAR, Cascini tried to identify different types of landslides using line-of-sight deformation [21]. Limited by the working principle of InSAR side-view imaging, the LOS displacement provided by single-track InSAR observations does not provide adequate support for landslide kinematic analysis. With the continuous enrichment of SAR images in recent years, it has become possible to integrate multi-angle radar observation LOS displacement to extract 2D displacements [22–24]. For example, Ren used ascending and descending track Sentinel-1 data to restore the vertical and east–west displacements of the Zaogutian landslide and discussed its mechanism [25]. Yi used the two-dimensional displacement information to study the activation mechanism of the Tangjiashan landslide [26]. Meng used the vertical and east–west displacements to identify and classify landslides in loess areas [27]. Existing studies detect the deformation characteristics of landslides moving along the east–west direction to the maximum extent by calculating the vertical and east–west displacements. However, for slopes with a non-east–west slip, the deformation characteristics are covered to some extent. The above factors lead to a significant difference between the recognition results of landslide kinematic features and natural deformation patterns.

Weining is located in the middle of China’s Yunnan–Guizhou Plateau and is an essential southern route of China’s West–East Power Transmission Project. As it is located in the transition zone between the first step of the Tibetan Plateau and the third step of the hilly eastern plain, tectonic activities and dissolution interactions are strong, and the slopes in the area are steep. In addition, the basaltic rocks developed in the large igneous province of Emei Mountain are widely distributed in the area [28]. Influenced by the subtropical monsoon climate, basaltic rocks undergo periodic hot and cold cycles and dry and wet cycles, forming weathering shells with high permeability and low strength. Landslide hazards are frequent in the study area due to the fragile geological environment, heavy rainfall and strong engineering disturbance [29–31]. Although researchers have conducted studies on active landslide identification and the deformation mechanism of catastrophic landslides, the link between the kinematic characteristics and deformation patterns has not been established.

In this paper, taking Weining as the study area, active landslides’ location and motion patterns are detected and identified using vertical and slope-oriented displacements. We acquired 82 Sentinel-1 images of ascending and descending tracks and processed them using the SBAS-InSAR method to obtain the boundaries of active landslides. The vertical and slope-oriented displacements are calculated by the two-dimensional decomposition equations. Based on this, the geomorphological features and the 2D displacement detected by InSAR are matched to achieve landslide motion pattern recognition. We identified 1 rotational slide, 10 planar traction slides, and 10 planar thrust slides in the study area. The accuracy of this method is verified by field investigations of three landslide cases. This study provides a solution for identifying motion patterns of landslides using geomorphic features and two-dimensional displacements acquired by InSAR, which is of great significance for geological hazard prevention.

## 2. Study Area

The study area is located in the western part of Guizhou Province, China, with an area of about  $6.3 \times 10^3$  km<sup>2</sup>. The area's elevation is high in the west and low in the east, ranging from 1240 m to 2880 m (Figure 1). The study area's north, west and south sides are cut by the Luoze River, the Niulan River and the Kedo River, respectively (Figure 2). Geotectonically, the study area is located at the southwest edge of the Yangzi platform, and the NNE-trending Shimen Fault, Haila Fault, and Zhaotong–Ludian Fault are developed in the area, with a length of more than 100 km (Figure 2). The study area is strongly eroded by river down-erosion and active fracture cutting, showing the characteristics of steep mountains and narrow river valleys. The study area has a subtropical monsoonal climate with an average annual precipitation of about 890 mm, and more than 90% of the rainfall is concentrated in April–October. Influenced by atmospheric circulation, rainfall increases from northwest to southeast.

The stratigraphic development in the study area is relatively complete, with outcrops from Proterozoic to Cenozoic strata, and the Permian strata are mainly developed (Figure 2). Among them, the Carboniferous (C) strata are mainly mudstone, sandstone and tuff; the Permian (P) strata are basalt, sandstone and mudstone; the Triassic (T) strata are mudstone, sandstone and tuff; and the Jurassic (J) strata are mudstone and sandstone. Influenced by the subtropical monsoon climate, basaltic rocks in the Permian strata undergo periodic hot and cold cycles and dry and wet cycles, forming thick layers of ancient weathering crusts, and are widely distributed in the study area. Although fresh basalts have high mechanical strength and low permeability, their strength and integrity are significantly reduced after intense weathering. Under rainfall and engineering disturbance, they are prone to sliding along the slope, causing geological disasters such as landslides and mudslides.

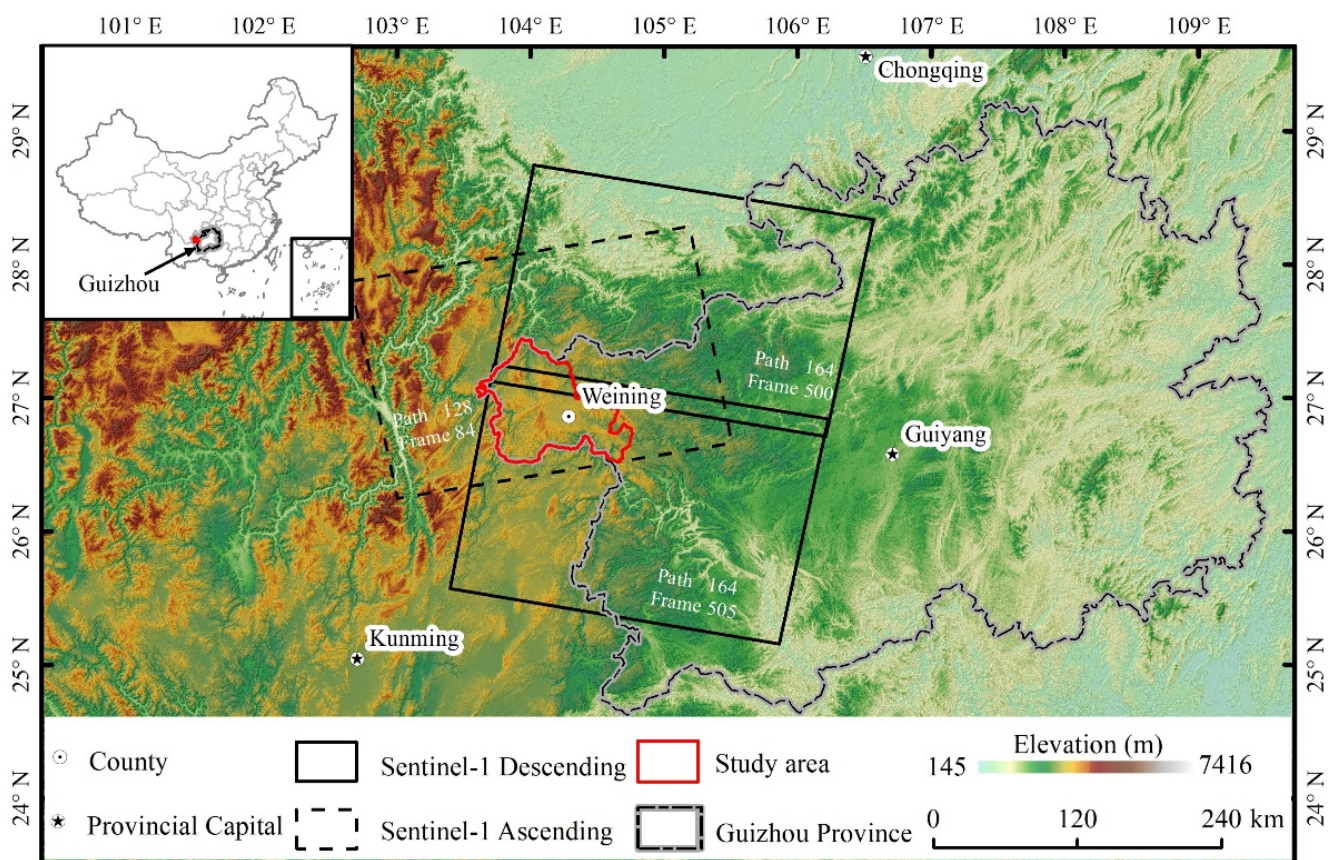
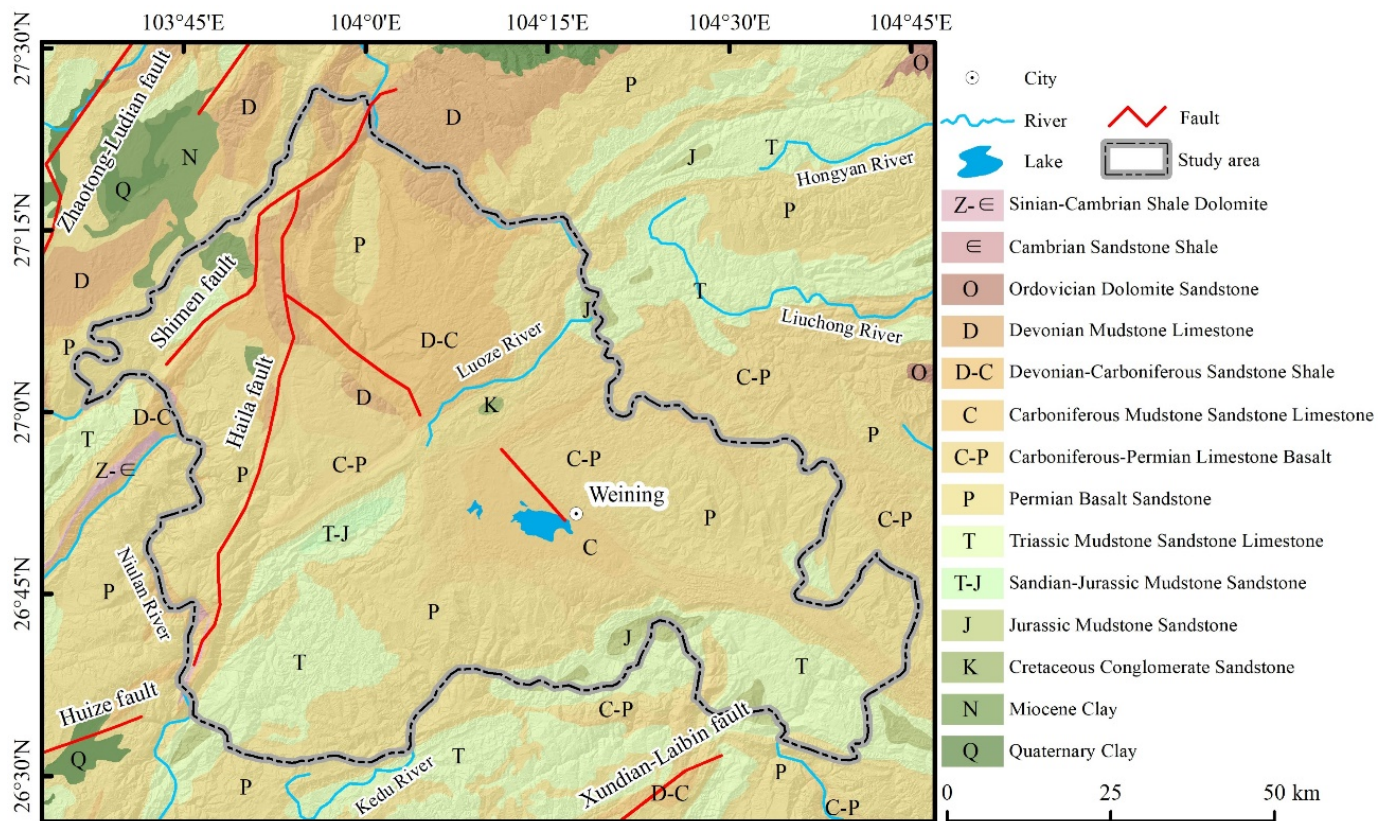


Figure 1. Geographic location of study area and SAR images coverage.



**Figure 2.** Geological map of the study area.

### 3. Datasets and Methodology

#### 3.1. Datasets

A total of 82 Sentinel-1 images of ascending and descending tracks taken from January 2019 to May 2020 were collected for displacement calculation in the study area. The ascending images have an incidence angle of  $39.64^\circ$  and an orbital azimuth of  $347.3^\circ$ , totaling 42 views; the descending images have an incidence angle of  $41.69^\circ$  and an orbital azimuth of  $196.53^\circ$ , totaling 40 views. The coverage of Sentinel-1 images is shown in Figure 1, and the detailed parameters of the radar images are shown in Table 1. ESA provided the precision orbital ephemeris data used for the interferometric calculations. The 1-arc-second digital elevation model (DEM) acquired by the Shuttle Radar Topographic Mapping Mission (SRTM) was used for geocoding, shadow coverage analysis, and geomorphological parameter calculation (aspect, slope and elevation). In addition to radar images, we collected sub-meter optical images and 3D terrain models from the Google Earth platform to assist in the identification of active landslides. Further, we obtained many landslide deformation photos during the field survey in November 2020, which were used to explain the landslide motion patterns. The stratigraphic lithology and fracture were obtained from the 1:200,000 geological map provided by the China Geological Survey. The rainfall data of the study area were downloaded from the Google Earth engine platform.

**Table 1.** Parameters of radar images used in the study.

Sensor	Wavelength	Direction	Path	Frame	Resolution (m)	Incidence Angle ( $^\circ$ )	Heading Angle ( $^\circ$ )	Number	Polarization	Temporal Coverage
Sentinel-1	5.6 cm	Ascending	128	84	$2.33 \times 13.96$	39.64	347.3	42	VV	9 January 2019–15 May 2020
		Descending	164	500,505	$2.33 \times 13.99$	41.69	192.56	40	VV	11 January 2019–5 May 2020

### 3.2. Methodology

This study integrated three indexes of geomorphic features as well as vertical and slope-oriented displacements, and proposed a kinematic analysis process for the weathered basalt landslide in Weining. The process consists of four steps: (I) Calculate the annual average LOS velocity and time-series displacement by the SBAS-InSAR method. (II) Identify active landslides using the annual average LOS velocity. (III) Using two-dimensional decomposition equations, calculate the annual average vertical and slope-oriented velocities and the time-series displacement. (IV) Using this method, we can effectively identify and classify the kinematic characteristics of an active landslide in the study area. On this basis, we conducted a field investigation on the identification results of typical landslides and verified the accuracy of the kinematic classification results. Furthermore, we discuss the relationship between rainfall and landslide deformation using time-series displacement. Finally, the uncertainty factors affecting the kinematic identification results of landslides are discussed. The flow chart of this study is shown in Figure 3.

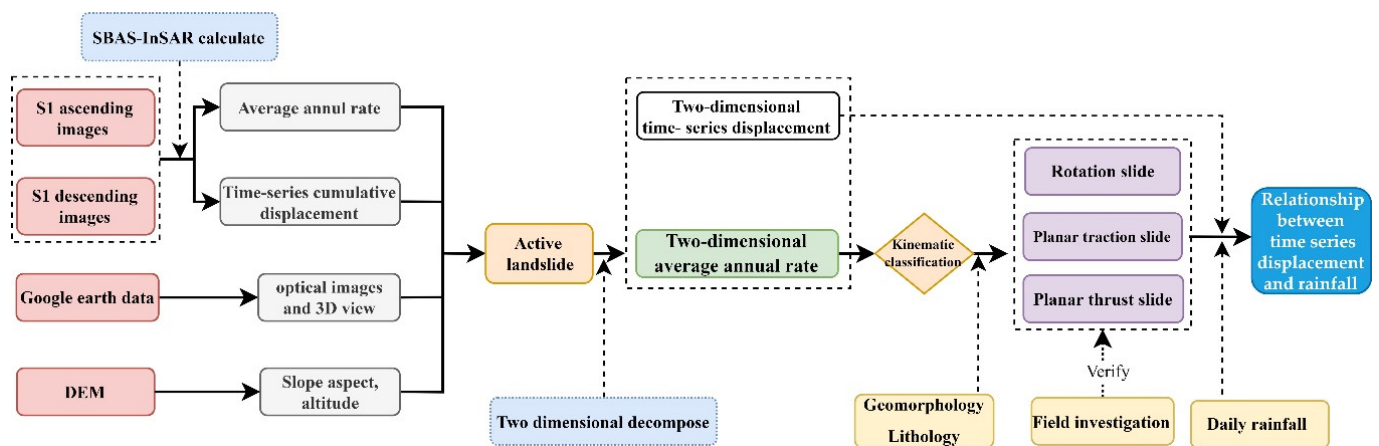


**Figure 3.** Research flow chart.

#### 3.2.1. SBAS-InSAR Processing

The SBAS-InSAR technique filters short spatial and temporal baseline interference combinations through a multi-master image strategy and extracts high-coherence point targets for the time-series analysis. The point target's time-series displacement and deformation rate can be obtained by a singular value decomposition of the unwrapped differential interference phase. This method overcomes the decorrelation problem caused by the long spatial and temporal baseline in the traditional D-InSAR technique and reduces the influence of atmospheric phase delay and elevation error [32]. This paper uses the SBAS-InSAR method to calculate the annual average deformation and time-series displacement.

First, we preprocessed the radar images. The radar images of ascending and descending tracks were coregistered to images acquired on 4 January 2020 and 25 December 2019, respectively. The signal-to-noise ratio of the interferograms was improved by multi-look factors of  $10 \times 2$ , and the ground direction resolution of the processed data was  $28 \text{ m} \times 28 \text{ m}$ .

Then, we optimized the interference combination and calculated the differential interference phase. The maximum temporal and spatial baseline were set to 48 d and 180 m, respectively. A total of 234 interferometric combinations were generated, including 120 sets of ascending and 114 sets of descending orbits (Figure 4). The wrap phase value was obtained by the differential interference calculation of the optimized interference combination.

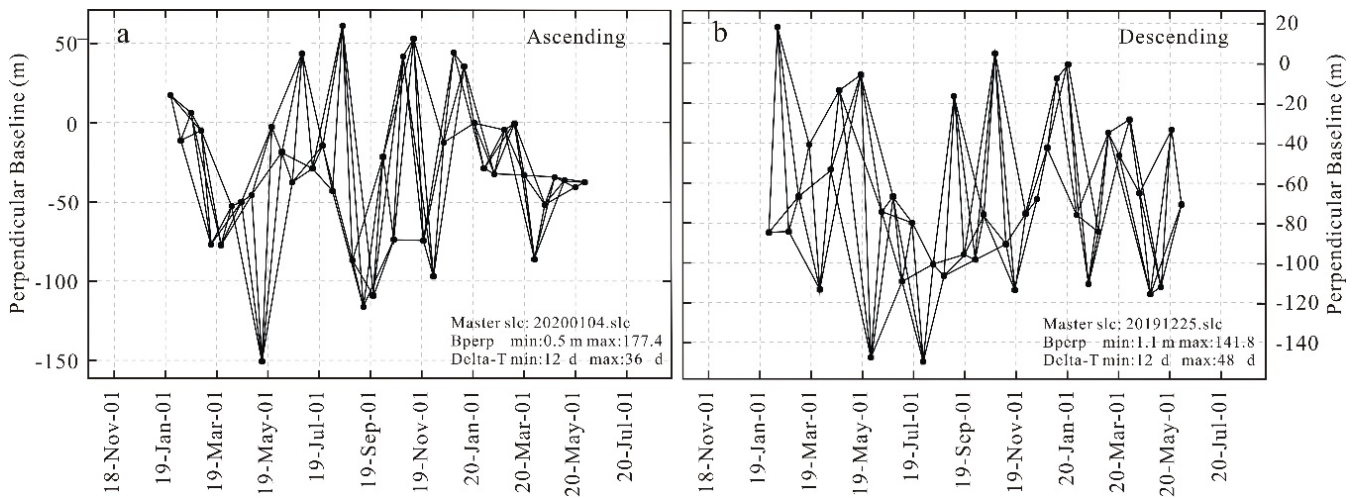


**Figure 4.** Interference combinations used in SBAS calculations. (a) Sentinel-1 ascending orbit; (b) Sentinel-1 descending orbit (black dots and lines indicate data acquisition dates and interference pairs, respectively).

Further, the minimum cost flow algorithm was used to unwrap the differential interference phase, and the unwrapping phases were superimposed to obtain the average deformation rate of the study area [33].

Finally, the correlation coefficients and standard deviations were used to extract high-quality coherence points. The atmospheric-induced phase errors were removed using an empirical linear elevation model and GACOS atmospheric products [34,35]. After removing the atmospheric errors, the singular decomposition method was used to calculate the unwrapping phases to obtain time-series displacements.

### 3.2.2. Two-Dimensional Displacement Decomposition

The LOS displacement can effectively serve for active landslide identification. However, in the kinematic analysis of landslides, the one-dimensional displacement cannot accurately portray the spatial motion characteristics. Theoretically, the three-dimensional displacement of the ground surface can be inferred by using the LOS deformation data in three incidence directions. However, due to the limitation of data coverage, it is difficult to obtain sufficient SAR data sets for 3D decomposition. Therefore, we calculated the vertical and horizontal displacements by combining the ascending and descending orbital LOS displacements. It should be emphasized that the horizontal direction was defined as the landslide sliding direction (slope-oriented) rather than the south–north or east–west direction. The two-dimensional displacement can be obtained by the following equation [24,36,37].

$$\begin{bmatrix} V_U \\ V_H \end{bmatrix} = \begin{bmatrix} \cos \theta_{As} & -\sin \theta_{As} \cos(\beta - \alpha_{As} + \frac{3\pi}{2}) \\ \cos \theta_{De} & -\sin \theta_{De} \cos(\beta - \alpha_{De} + \frac{3\pi}{2}) \end{bmatrix}^{-1} \cdot \begin{bmatrix} V_{As} \\ V_{De} \end{bmatrix} \quad (1)$$

$V_U$  and  $V_H$  are the displacement in the vertical and sliding directions.  $V_{As}$  and  $V_{De}$  are the LOS displacements in the ascending and descending orbits.  $\alpha_{As}$  and  $\alpha_{De}$  represent the azimuths of the ascending and descending satellite flights.  $\beta$  is the azimuth of the slope sliding direction.  $\theta_{As}$  and  $\theta_{De}$  represent the satellite incidence angles. The projection relationship between the direction of radar flight and the direction of ground motion is shown in the Figure 5.

### 3.2.3. Classification of Landslide Motion Pattern

Varnes and Hungr proposed classical landslide-classification criteria based on the material composition and landslide motion characteristics of landslides, which have been widely

accepted by researchers [38,39]. Based on Varnes and Hungr's landslide-classification criteria, this paper integrates three indicators of landslide geomorphic features, vertical displacement rate, and slope-oriented displacement rate, and proposes a remote sensing identification method for landslide motion patterns. The identification characteristics of rotational slides, planar traction slides and planar thrust slides are as follows:

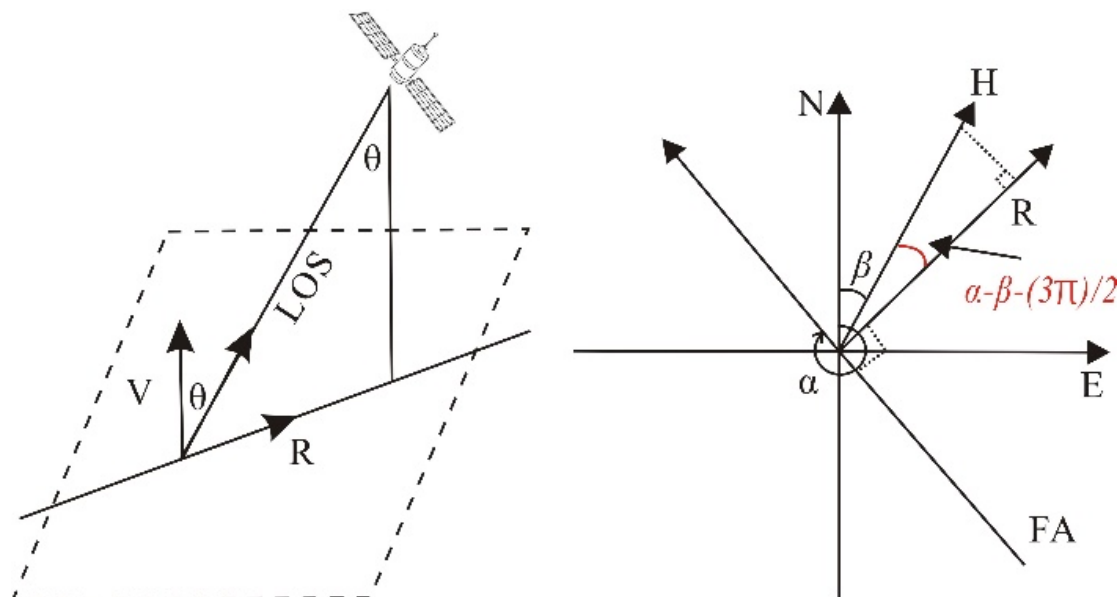


**Figure 5.** Schematic diagram of the projection of the radar flight direction and the surface movement direction; V is the vertical projection direction, R is the range direction, H is the slope sliding direction, and FA is the radar flight direction (modified after [36]).

**Rotational slide:** For rotational landslides, the sliding surface is up-concave, and the landslide moves approximately around the axis parallel to the slope. This type of landslide is mainly developed in a thick layer of strongly weathered basalt, and the burial depth of the rupture surface is relatively deep (usually more than 100 m) [40,41]. Its scale is generally larger than that of planar landslides. The rupture surface of rotational slides is mainly affected by faults and joints. This type of landslide is mainly located on the river bank in the study area. In the process of river erosion, vertical and horizontal shear stresses occur at the top and foot of slopes. Under the joint action of farmland irrigation at the head and river cutting at the foot of the landslide, the internal joint surface of the slope penetrates and forms an arc-shaped sliding surface and then undergoes integral sliding deformation. The landslide consists of a head, main body and foot. For the rotational slide, the horizontal displacement velocity is similar to the vertical displacement velocity, but the spatial distribution characteristics are different. The dominant deformation in the head is downward vertical displacement, but its horizontal displacement is small. In the transition from head to foot, the vertical displacement rate gradually decreases and the horizontal displacement rate gradually increases. In the main body, the horizontal and vertical displacement rates reach equilibrium. The deformation in the foot is dominated by horizontal displacement, while the downward vertical displacement is small (Figure 6a,b).

**Planar traction slide:** The sliding surface of a planar slide is linear, and the landslide moves along a plane parallel to the slope. This type of landslide is mainly developed in strong-medium weathered basalt. The rupture surface of a planar slide is shallow, usually less than 50 m. The rupture surface is influenced by rock joints and fissures and is usually the weak structural surface between the strongly and moderately weathered basalt [42–44]. The main deformation area of a planar traction slide is located at the foot of the landslide. Under the disturbance of river erosion, farmland irrigation or road cutting, the maximum principal stress at the foot of the landslide is nearly horizontal and the minimum principal

stress is nearly vertical. The sliding rupture surface arises at the  $45-\varphi/2$  intersection angle in the direction of the first principal stress [45,46]. It continues to expand and penetrate the soft structural surface between the strongly weathered and moderately weathered basalt, and eventually slides monolithically under the traction of the landslide foot. The dominant deformation of planar traction slides is in the horizontal direction. The maximum vertical displacement rate is located in the foot. The vertical displacement rate gradually increases when transitioning from the head to the foot of landslides. The horizontal displacement rate value does not significantly change and is always larger than the vertical deformation (Figure 6c,d).

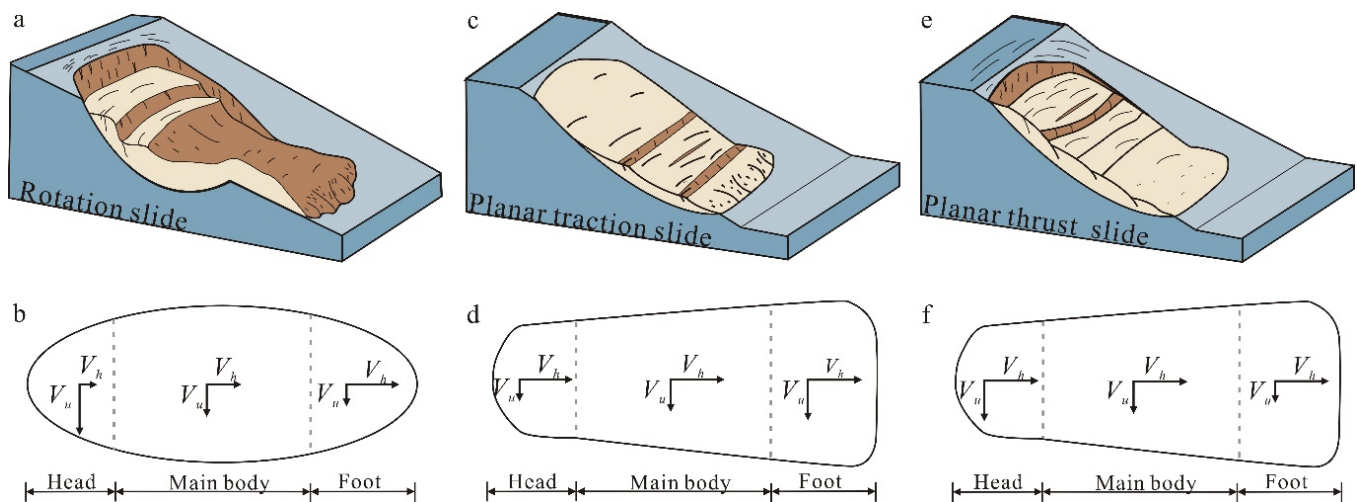


**Figure 6.** (a) Schematic diagram of rotational slide; (b) plane velocity distribution of rotational landslide; (c) schematic diagram of planar traction slides; (d) plane velocity distribution planar traction slide; (e) schematic diagram of planar thrust slide; (f) plane velocity distribution of planar thrust slide;  $V_u$  is vertical displacement velocity,  $V_h$  is horizontal (slope-oriented) velocity (modified after [26,39]).

**Planar thrust slide:** The main deformation area of the planar thrust slide is located at the head of the landslide. The shear strength of weathered basalt decreases significantly due to irrigation and rainfall at the head of landslides, which results in creep deformation at the head and pushes the slope slide downward [47,48]. The cracks and staggered steps in the heads of landslides provide a good channel for water to enter the rupture surface, and the entry of the water further accelerates the weakening of the shear strength of the rupture surface, which eventually leads to the overall sliding of the slope along the weak structural surface. The dominant deformation of planar thrust slides is in the horizontal direction. Unlike planar traction slides, the maximum vertical displacement rate of planar thrust slides is located in the head. In the transition from the head to the foot of landslides, the vertical displacement deformation gradually decreases, and the value of the horizontal displacement rate does not significantly change and is always larger than the vertical deformation (Figure 6e,f).

## 4. Results and Analysis

### 4.1. Active Landslide Identification

According to the process described in Section 3.2.1, we obtained the annual average deformation of ascending and descending orbits in the study area. Integrating the annual average deformation rates of ascending and descending tracks, multi-temporal optical remote sensing images and geomorphological information, we identified 20 active landslides in the study area. The location of the landslides is shown as a solid white circle in Figure 7. To show the ground deformation of the study area in detail, we highlighted some of the

deformation areas (Figure 7a–e). Positive displacement indicates movement toward the radar and negative displacement indicates movement away from the radar.

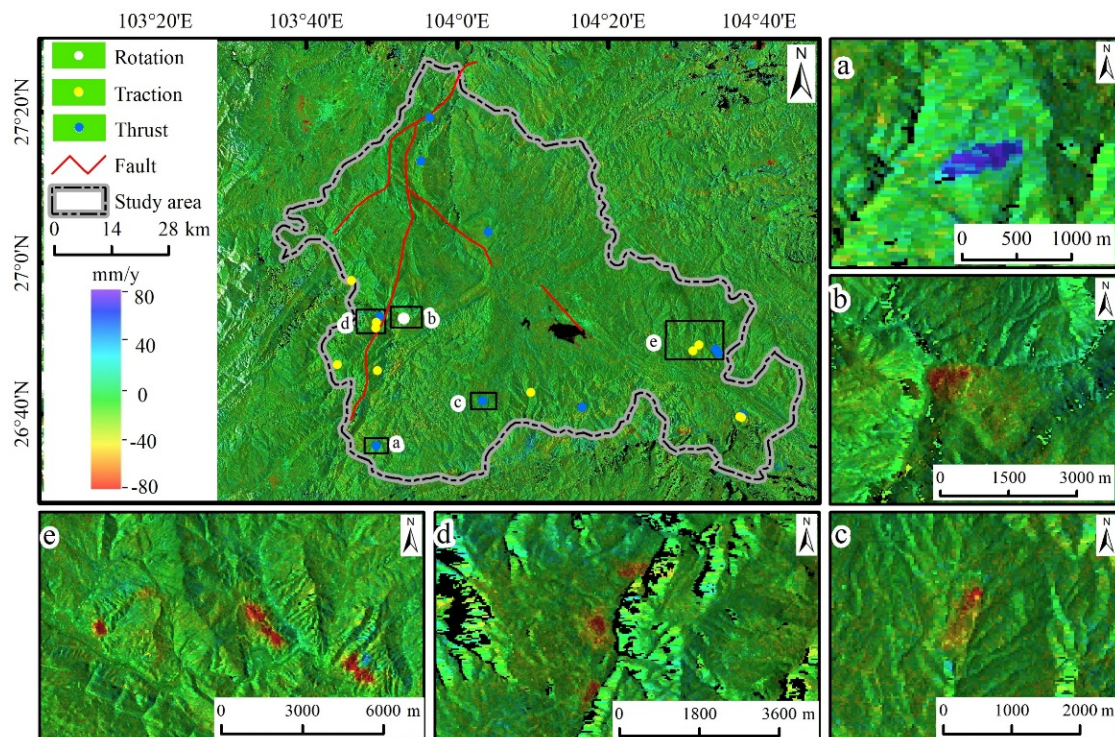


**Figure 7.** Active landslide distribution in Weining. The solid circles are the locations of active landslides, and the base diagram is the average annual displacement rate obtained by the descending images. (a–e) show the partial enlargements. (In order to better show the landslide boundaries, only the displacement between  $-80$  mm/y to  $80$  mm/y is shown, and it should be emphasized that there are still very few areas with displacement velocities over  $\pm 150$  mm/y).

The distribution map of active landslides shows that the landslides are mainly located in the east (areas b, d) and west (area e) of the study area and are more discrete in the south (areas a, c). The active landslides are mainly concentrated in the slope areas with deep geomorphic cuts, and 70% of the active landslides have slopes between  $20^\circ$  and  $30^\circ$ . The central part of the study area is flat, so the number of landslides detected on the west and south sides is much larger than that in the central and northeastern parts of the study area, as shown in areas a–e in Figure 7. In addition, the number of developed landslides is significantly and positively correlated with the distance from the active fault because the rock near the fault is more fragmented, severely weathered, and steeper in topography. A total of 11 active landslides, accounting for 55%, were identified within 20 km of the Haila Fault on the west side of the study area.

We conducted field investigations on the detected active landslides. All of the landslide surfaces had developed different degrees of deformation phenomena, such as cracks, steep landslide bumps and collapses in the leading edge. There are 16 landslides close to residential areas, and the continuous deformation of the landslides seriously threatens the residents' production and living safety. We found that the active landslides are mainly developed in the Permian and Triassic strata. The characteristic lithology of the strata is strongly weathered basalt and sand mudstone. They have high porosity and low rock integrity and strength. According to previous studies and site investigations, these weathered materials can be up to nearly 100 m thick. Therefore, under the action of external conditions, these active landslides usually slide along the slope direction, causing catastrophic landslide events.

#### 4.2. Validation of Landslide Motion Pattern

Combing the active-landslide-detecting results and the slope information extracted from the digital elevation model, we identified the movement direction of 21 active landslides. The landslides' movement directions were verified by the high-precision optical remote sensing images. We generated horizontal and vertical rate maps of the active landslides using the two-dimensional displacement decomposition equation (Equation (1)) and identified the landslide motion patterns. A total of 1 rotational slide, 10 planar thrust slides and 10 planar traction slides were identified in the study area. The landslide locations and detailed information are shown in Figure 7 and Table 2.

**Table 2.** Characteristics of active landslides detected by InSAR in the study area.

Landslide Number	Landslide Name	Longitude (°)	Latitude (°)	Length (m)	Width (m)	MHV (mm/y)	MVV (mm/y)	$\beta$ (°)	Kinematic Type
L <sub>04</sub>	Xiamatian	103.882	26.877	860	900	49	50	260	R
L <sub>03</sub>	Bainijing	103.765	26.961	380	720	41	19	215	P-TR
L <sub>05</sub>	Jieli	104.521	26.806	710	840	66	34	203	P-TR
L <sub>06</sub>	Liujiagou	104.533	26.818	1180	840	78	46	309	P-TR
L <sub>10</sub>	Hanjiaping	103.821	26.869	890	1050	57	32	80	P-TR
L <sub>11</sub>	Dapingzi	103.819	26.855	460	790	69	39	110	P-TR
L <sub>12</sub>	Zhande	103.823	26.762	980	730	40	30	99	P-TR
L <sub>13</sub>	Songlingping	103.735	26.775	470	1160	72	35	318	P-TR
L <sub>16</sub>	Dakouzi	104.162	26.713	870	410	59	35	156	P-TR
L <sub>18</sub>	Yanzutian	104.624	26.660	300	427	71	31	220	P-TR
L <sub>19</sub>	Shiyakou	104.627	26.659	312	550	89	37	205	P-TR
L <sub>01</sub>	Dahaizi	103.939	27.321	1120	320	76	55	357	P-TH
L <sub>02</sub>	Xujiayan	103.920	27.224	1360	500	78	31	48	P-TH
L <sub>07</sub>	Xiaohe	104.068	27.068	850	350	53	30	300	P-TH
L <sub>08</sub>	Wachang	104.276	26.681	620	280	57	23	170	P-TH
L <sub>09</sub>	Wujiapingzi	103.828	26.881	980	600	54	30	66	P-TH
L <sub>14</sub>	Sanjiacun	103.821	26.596	998	450	68	28	240	P-TH
L <sub>15</sub>	Laoyaying	104.055	26.695	1300	360	128	59	208	P-TH
L <sub>17</sub>	Tuojiyuanzi	104.629	26.665	733	790	67	46	275	P-TH
L <sub>20</sub>	Dongfeng	104.577	26.801	415	910	149	60	217	P-TH
L <sub>21</sub>	Sanguozhuang	104.570	26.809	900	500	98	66	290	P-TH

MHV: maximum horizontal velocity; MVV: maximum vertical velocity;  $\beta$ : the azimuth of slope sliding direction; R: rotational slide; P-TR: planar traction slide; P-TH: planar thrust slide.

##### 4.2.1. Rotational Slide

The rotational landslide is dominated by the head's vertical and the foot's horizontal displacement, and the slope moves along an arc-shaped sliding surface. In this paper, we used the Xiamatian (XMT) landslide as an example to verify the results of rotational landslide identification.

The XMT landslide is located on the west side of the study area, about 4 km from the southwest direction of the Haila Fault. It is 860 m long and 900 m wide, with an area of about 0.64 km<sup>2</sup>. The landslide is convex in plan with a surface elevation varying from 1560 m to 1760 m. The average slope gradient of the landslide is 25°, and the slope aspect is about 260°. The main body of the slope develops several gullies with a width of more than 20 m and a depth of about 10 m (Figure 8a). The primary material forming the

landslide is weathered basalt, about 100 m thick, with high porosity, poor rock integrity and low strength.

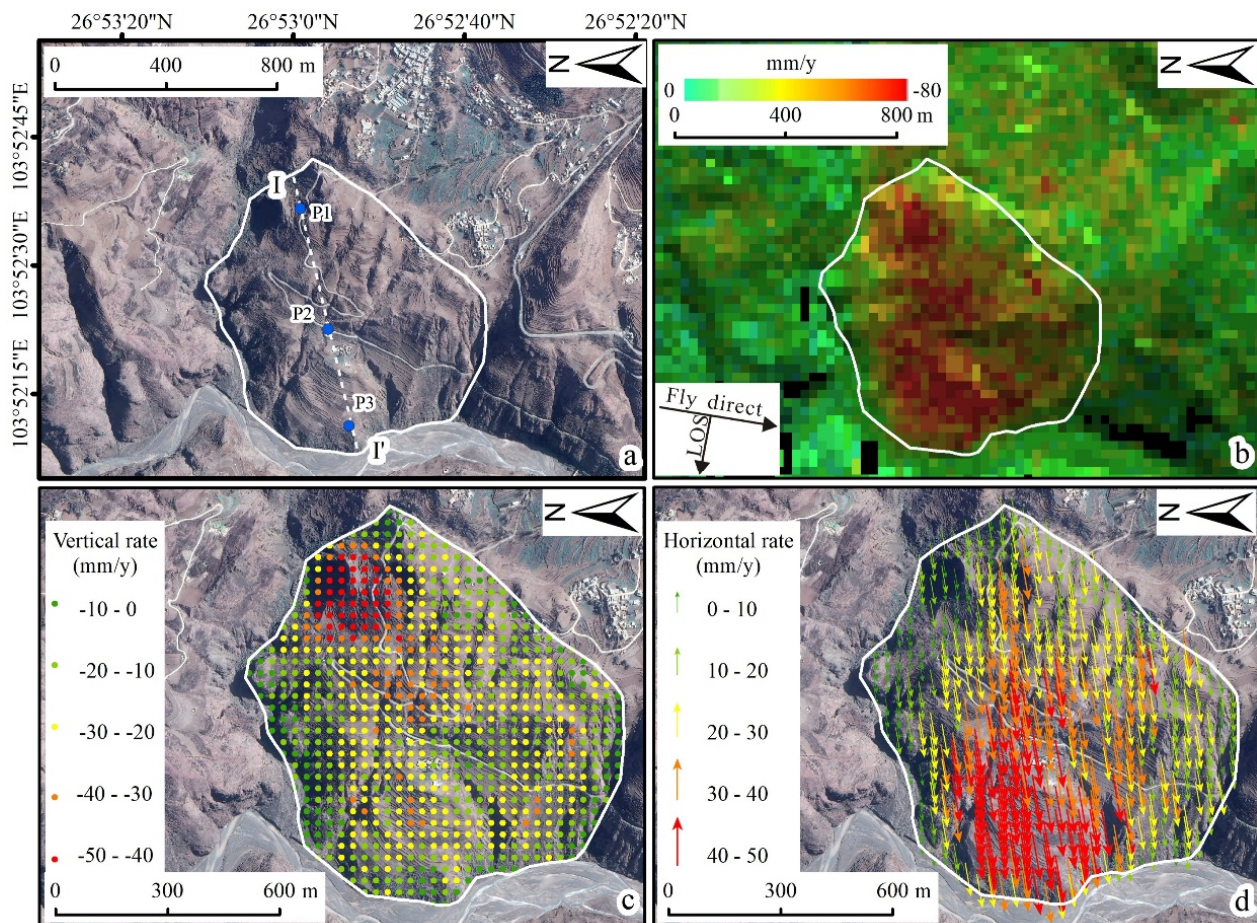


**Figure 8.** (a) Overview of XMT landslide; (b) annual average displacement in LOS direction obtained from Sentinel-1 descending images; (c) vertical rate; (d) horizontal rate.

The XMT landslide is sparsely vegetated, and the Sentinel-1 images from ascending and descending orbits provide valid measurements. Figure 8b shows the annual average LOS displacement rate of the XMT landslide obtained by descending images. The XMT landslide has prominent overall deformation characteristics, and its maximum LOS displacement rate is about  $-80$  mm/y. Along the vertical direction of the landslide movement, the displacement rate gradually decreases. We obtained the landslide boundary by combining the annual average displacement rate and optical images.

In order to quantitatively evaluate the two-dimensional deformation characteristics of the XMT landslide, we calculated the vertical and horizontal rates. The results show that the maximum vertical and horizontal rates are in the same range, which is  $40$ – $50$  mm/a (Figure 8c,d). However, there are differences in the spatial distribution characteristics of the vertical and horizontal rates. The maximum vertical rate is  $-50$  mm/a at the head of the landslide along the landslide movement direction, the vertical rate gradually decreases, and the rate decreases to  $-20$  mm/a at the foot (Figure 8c). On the contrary, the horizontal velocity at the foot of the landslide is the largest and gradually decreases along the slope (Figure 8d). In the main body, the vertical and the horizontal rates are equal.

The field investigations found that the XMT landslide had multiple macroscopic deformation phenomena. Large-scale vertical dislocation occurred at the head of the landslide, and the failure surface was concave. Multiple landslide steps were developed, with a maximum vertical dislocation distance of about 2 m. The deformation in this area is mainly vertical displacement, accompanied by smaller-scale horizontal displacement. A

nearly upright landslide back wall has developed at the back edge of the landslide. The outcrop lithology is yellow–brown weathered basalt, with a broken structure and poor mechanical properties (Figure 9b). In the main body of the landslide, multiple nearly parallel tension cracks have developed with a width greater than 20 cm and an NW20° orientation, accompanied by small-scale vertical displacement (Figure 9c). In addition, tension cracks were also observed to varying degrees in the hardened roads and buildings in the main body of the landslide. The deformation in the main body of the landslide has a smaller distribution and lower degree compared with the deformation in the head and foot of the landslide. This phenomenon is consistent with the two-dimensional displacement rate distribution characteristics obtained from the InSAR observations. A number of tension cracks with a width of more than 50 mm developed on the surface of the farmland and slope at the foot of the landslide towards NW30°–40°. In addition, five small collapses developed at the landslide’s foot (Figure 9d). We found that there are still dozens of residential buildings on the landslide body, and the continuous deformation of the landslide poses a severe threat to them.

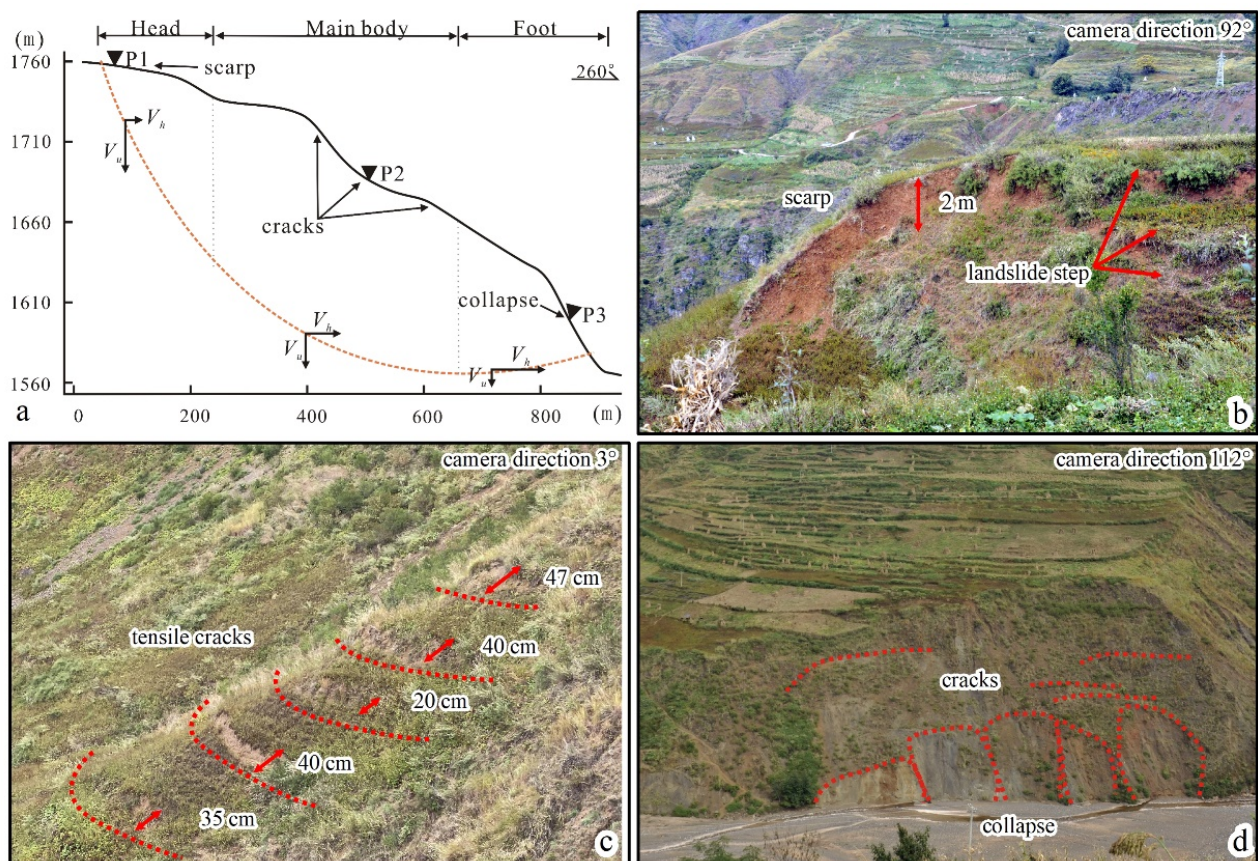


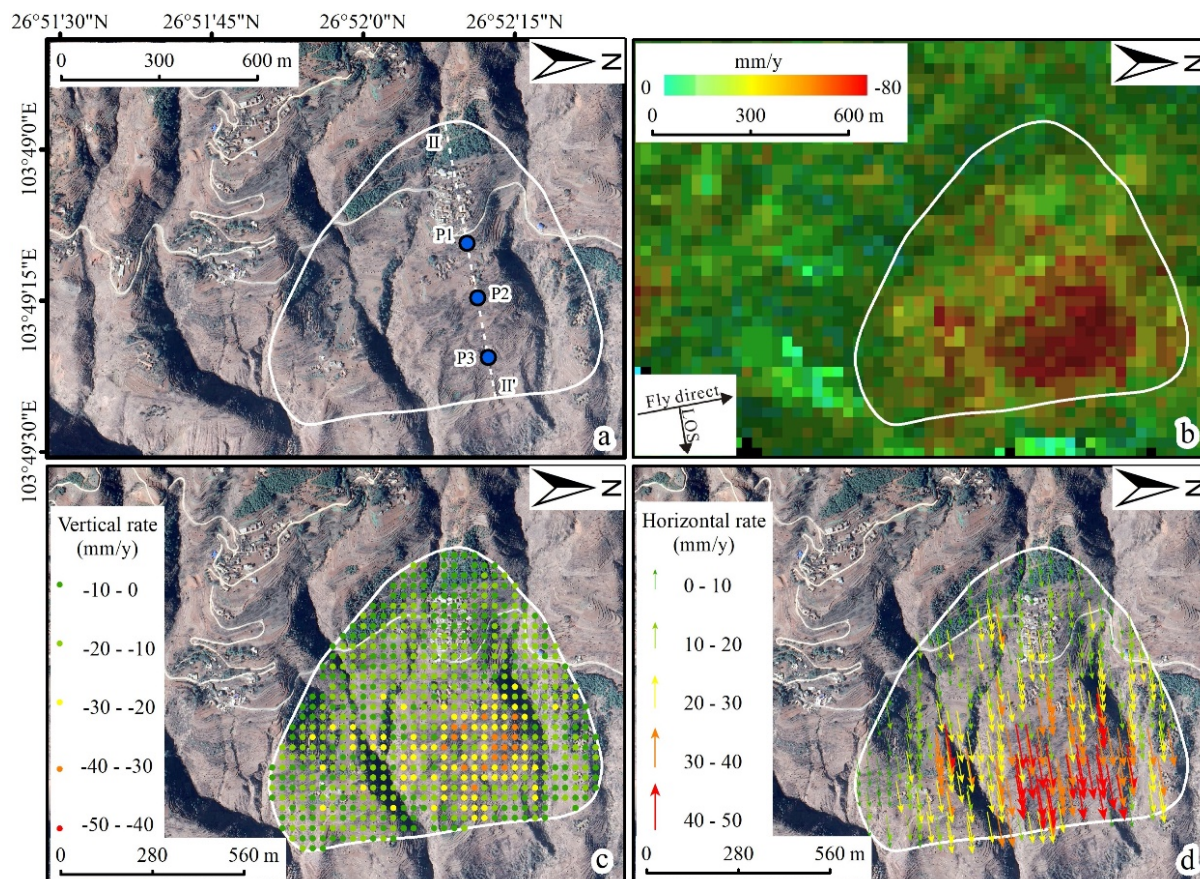
**Figure 9.** (a) Landslide profile I-I' and location of field survey points; (b) deformation in the head of XMT landslide (corresponding to point P1); (c) tension cracks in the main body of XMT landslide (corresponding to point P2); (d) tension cracks and small collapse at the foot of XMT landslide (corresponding to point P3).

#### 4.2.2. Planar Traction Slide

The dominant deformation of planar traction slides is in the horizontal direction. The maximum vertical displacement rate is located in the foot. The slope slides along the plane as a whole by foot traction. In this paper, we used the Hanjiaping (HJP) landslide as an example to verify the planar traction slide identification results.

The HJP landslide is located 6 km west of the Xiaomata landslide. It is 890 m long and 1050 m wide, with an area of 0.62 km<sup>2</sup>. The landslide is fan-shaped in the plan, with a

surface elevation of 1900–2080 m. The average slope of the landslide is  $30^\circ$  and the slope aspect is about  $80^\circ$ . The back edge of the landslide is chair-shaped, and two gullies cut the main body with a width of about 150 m and a depth of about 32 m (Figure 10a). The main material of the landslide is weathered basalt, and the thickness of the slide is about 50 m.



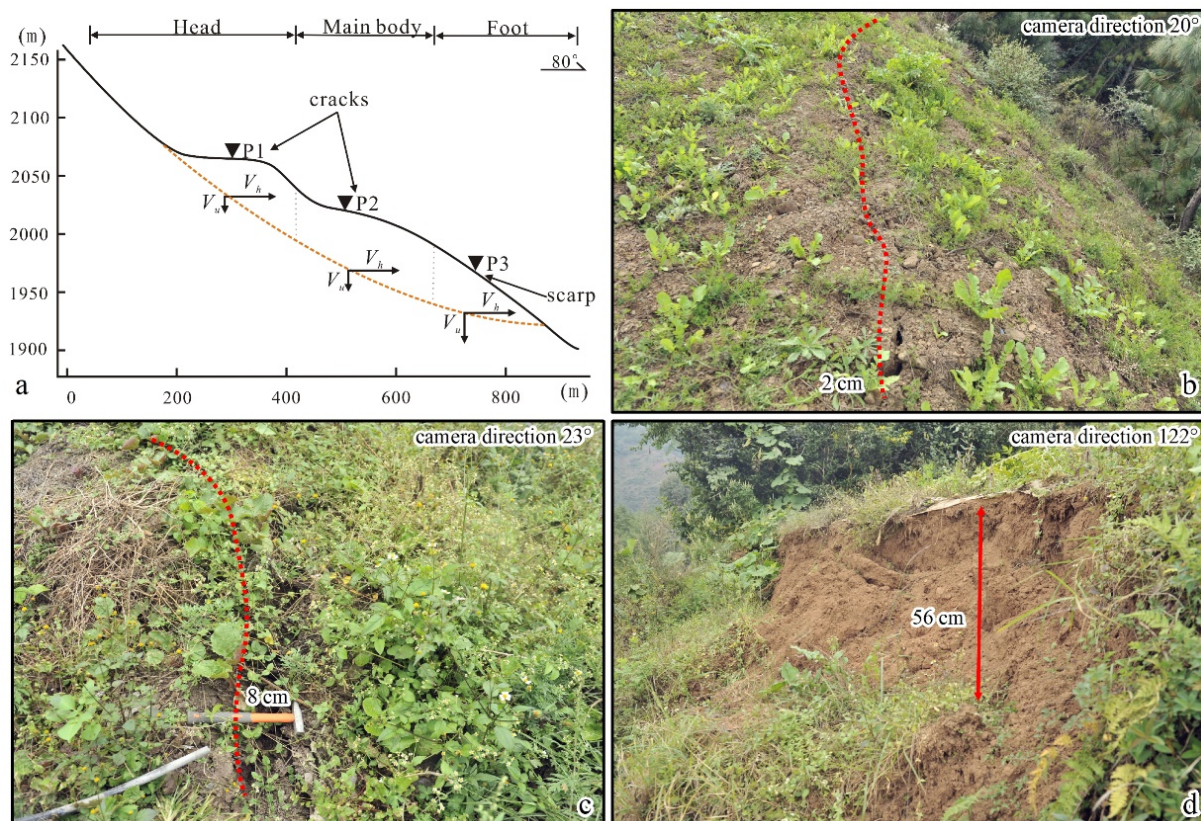
**Figure 10.** (a) Overview of HJP landslide; (b) annual average displacement in LOS direction obtained from Sentinel-1 descending images; (c) vertical rate; (d) horizontal rate.

Figure 10b shows the annual average LOS displacement rate of the HJP landslide obtained by Sentinel-1 descending images. The results show that the landslide has signs of overall deformation. The high displacement rate is mainly concentrated at the foot of the landslide, where the displacement rate reaches  $-80$  mm/y, decreasing as the altitude increases. The annual average displacement rate and the optical images were integrated, and the landslide boundary was detected (Figure 10b).

The two-dimensional displacement decomposition results show that the maximum horizontal deformation is located at the foot of the landslide with a rate of  $50$  mm/a, and the average horizontal rate of the slope surface is  $43$  mm/a (Figure 10c,d). The maximum vertical deformation is located at the foot with a rate of  $-30$  mm/a, and the average vertical displacement rate at the foot is  $-22$  mm/a. The vertical rate gradually decreases upward along the slope (Figure 10c). The horizontal rate changes less in the main body of the landslide (near point P2), but the vertical rate decreases significantly. On the whole, the landslide is dominated by horizontal deformation.

The field survey found a small number of tension cracks with a width of about 2 cm and a length of about 8 m developing at the head of the landslide (P1), with a strike of  $NE0^\circ-5^\circ$  (Figure 11b). In the main body of the landslide, the number and width of fractures increase significantly, accompanied by vertical dislocation. A tensile crack with a strike of  $NE2^\circ-6^\circ$ , a width of 5–8 cm and a length of 10 m was observed at position P2 (Figure 11c). The foot of the landslide has significant vertical deformation, with multiple

vertical misalignment steps and deep tension cracks. A staggered step was observed at the location of P3, accompanied by tension cracks. The staggered step distance is 56 cm, and the strike is  $5^{\circ}$ – $10^{\circ}$ NE. The exposed rock is a yellow–brown weathered basalt (Figure 11d). The field investigation results show that the overall deformation of the HJP landslide is mainly horizontal tension fractures. The slope is pulled by the foot and gradually develops to the head, producing a monolithic movement. This phenomenon is consistent with the two-dimensional kinematic characteristics observed by InSAR.



**Figure 11.** (a) Landslide profile II-II' and location of field survey points; (b) deformation in the head of HJP landslide (corresponding to point P1); (c) tension cracks in the main body of HJP landslide (corresponding to point P2); (d) tension cracks and small collapse at the foot HJP landslide (corresponding to point P3).

#### 4.2.3. Planar Thrust Slide

The dominant deformation of planar thrust slides is in the horizontal direction. The maximum vertical displacement rate is located in the head. The deformation of unstable material at the head of the landslide thrusts the slope rock mass to slide along the plane as a whole. In this paper, we used the Laoyaying (LYY) landslide as an example to verify the planar traction slide identification results.

The LYY landslide is located in Sanjia Village, south of the study area. It is 1300 m long and 360 m wide, with an area of  $0.49 \text{ km}^2$ . The landslide is tongue-shaped, with a surface elevation of 2220 m–2350 m and a top-toe elevation difference of 130 m. The average slope of the landslide is  $15^{\circ}$ , and the overall slope aspect is about  $208^{\circ}$ . It is located in a concave valley, and the terrain on both sides of the landslide is higher than the landslide body. Weathered basalt is the primary material forming the landslide (Figure 12a).

Figure 12b is the annual average LOS deformation rate of LYY landslide observed by Sentinel-1 descending images. The results show that the landslide has signs of overall deformation. The high displacement rate is concentrated at the head of the landslide, with

the maximum LOS rate greater than  $-100$  mm/y. We detected the landslide boundary by integrating the annual average LOS rate and optical images (Figure 12b).

The average horizontal rate of landslide surface is 63 mm/a, and the average vertical rate is 23 mm/a. The dominant deformation is in the horizontal direction. Along the downward slope aspect direction, the divergent characteristics of the horizontal velocity of landslide are not obvious (Figure 12c,d). The horizontal rate gradually increases from the eastern to the western boundary. The maximum vertical rate is located at the head, with a displacement rate of  $-45$  mm/a. Along the downward slope aspect direction, the vertical rate gradually decreases. In the main body of the landslide, the vertical rate is about  $-23$  mm/a, which is much smaller than the horizontal rate.

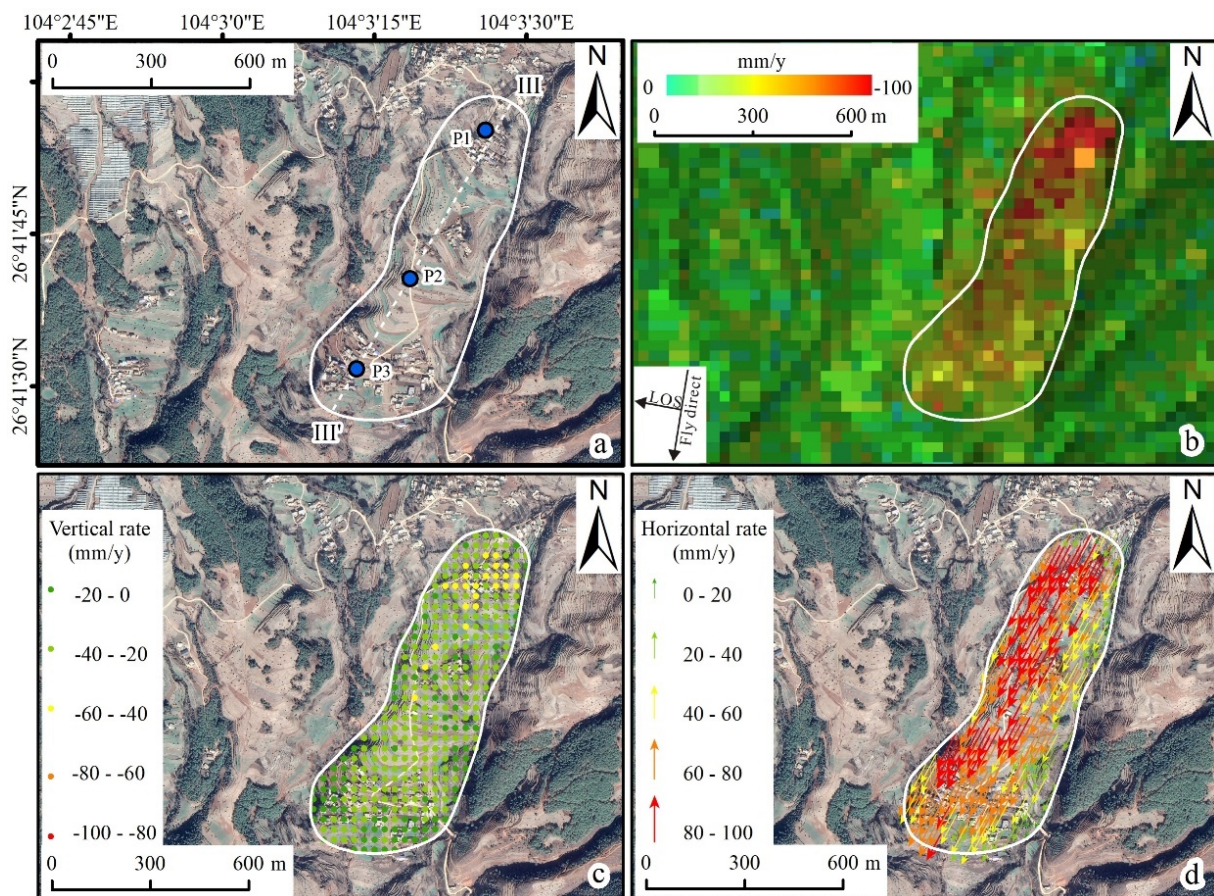


**Figure 12.** (a) Overview of LYY landslide; (b) annual average displacement in LOS direction obtained from Sentinel-1 descending images; (c) vertical rate; (d) horizontal rate.

The field investigation found significant deformation at the head of the landslide. The hardened road had developed multistage steps, of which the maximum vertical displacement is 15 cm and width is 30 cm. The crack extends from the road to the farmland on both sides, with a length of more than 20 m and a direction of  $NW53^{\circ}$ – $60^{\circ}$  (Figure 13b). The road in the main body of the landslide develops a large number of subparallel cracks, and the vertical deformation phenomenon is not apparent. The width of the cracks varies from 2–5 cm, with the strike of  $NE20^{\circ}$ – $40^{\circ}$ . They intersect diagonally with the landslide sliding direction. Pinnate cracks were observed in hardened pavement cracks, which are presumed to be shear cracks caused by horizontal velocity differences (Figure 13c). The width and number of cracks decrease from the head to the foot of the LYY landslide. A few cracks with a strike of  $NW50^{\circ}$ – $70^{\circ}$  and a width of about 1 cm were observed on buildings at the foot of the LYY landslide (Figure 13d). The deformation phenomena investigated in the field are consistent with the 2D kinematic features acquired by InSAR.

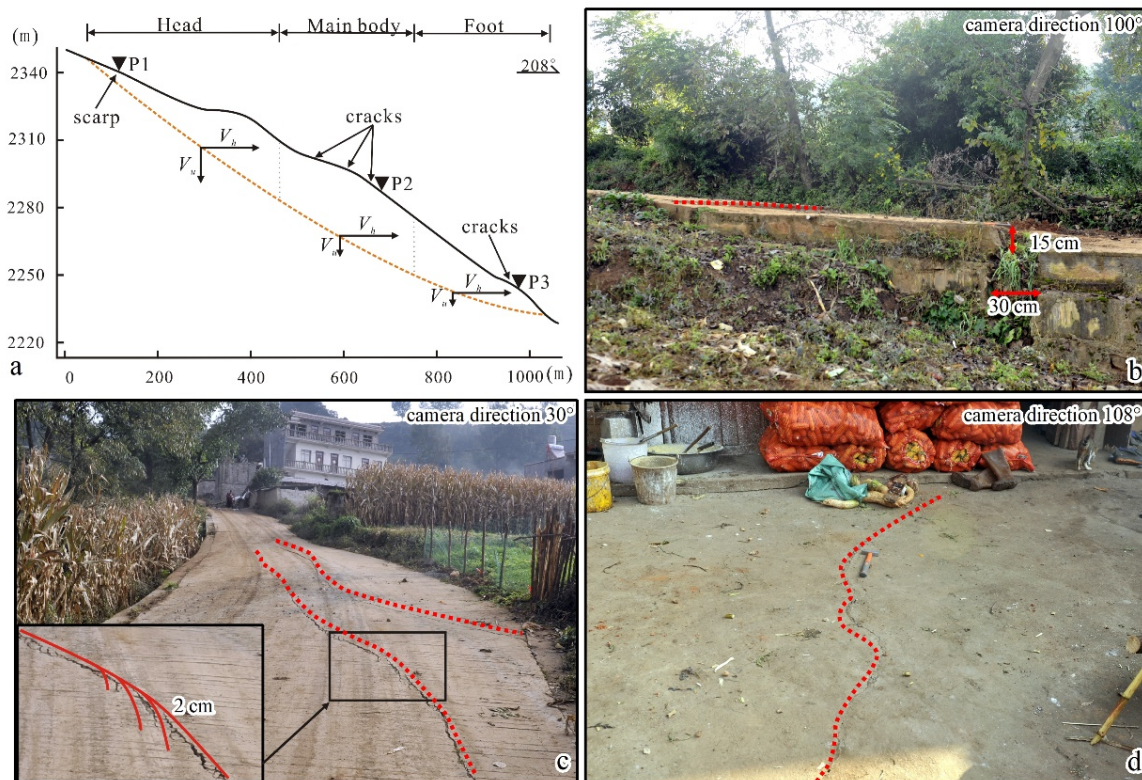


**Figure 13.** (a) Landslide profile III-III' and location of field survey points; (b) deformation in the head of LYY landslide (corresponding to point P1); (c) shear cracks in the main body of LYY landslide (corresponding to point P2); (d) tension cracks and small collapse at the foot HJP landslide (corresponding to point P3).

## 5. Discussion

### 5.1. Relationship between Time-Series Displacement of Landslides and Rainfall

Based on the two-dimensional decomposition equation and the SBAS-InSAR observation results, we obtained typical landslides' vertical and horizontal time-series displacements. The time-series displacement and daily rainfall data were matched by time to discuss the correlation between rainfall and landslide deformation. The rainy season in the study area is from April to October, and rainfall in the rainy season accounts for more than 90% of the year. Figure 14a–f show the vertical and horizontal time-series displacements of the landslides in XMT, HJP and LYY, respectively.

The XMT landslide and the HJP landslide are close to each other and have the same regional rainfall characteristics. The horizontal displacement rate of the XMT landslide increased significantly from April 2019 (Figure 14b), and its vertical displacement acceleration was slightly delayed (Figure 14a). Two concentrated rainfall events occurred in August and October 2019, and the horizontal and vertical displacements of the XMT landslide both showed obvious accelerated characteristics (Figure 14a,b). The horizontal rate of the HJP landslide also accelerated after the concentrated rainfall event in October 2019 (Figure 14d). During the rainy season, the horizontal and vertical displacements of the monitored points on the XMT landslide account for 65% and 68% of the total annual displacements, respectively. The horizontal displacement of HJP landslide accounts for about 61% of the annual displacements.

The LYY landslide was affected by persistent precipitation from June 2019. The horizontal and vertical displacements showed significant acceleration characteristics, and the nodes of accelerated deformation coincided with the appearance of high precipitation values (Figure 14e,f). At the end of the rainy season in October 2019, the landslide was still in a state of continuous deformation, but there was no sign of acceleration.

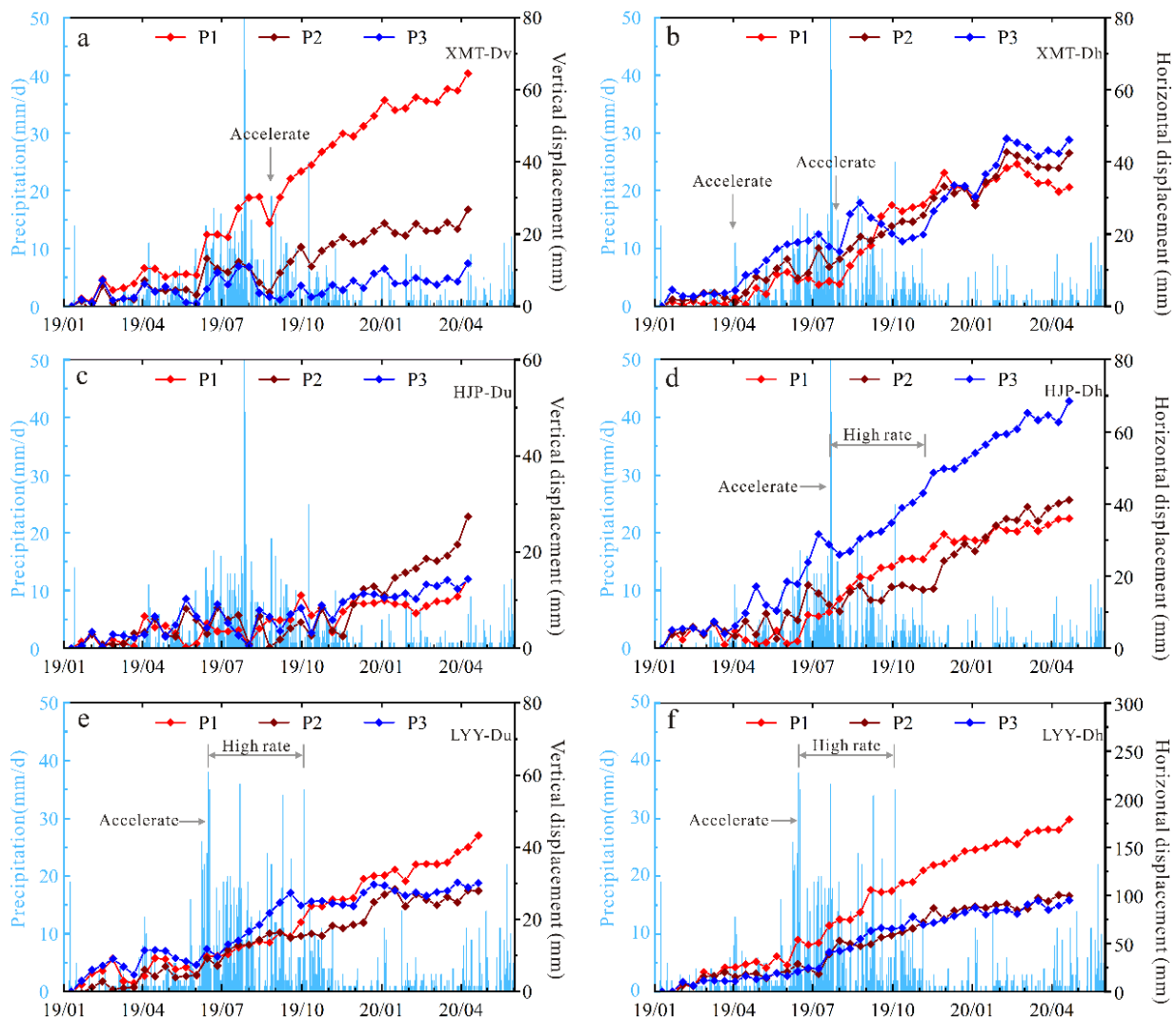


**Figure 14.** Time-series displacement of typical landslides' monitoring points with daily rainfall. (a) Vertical displacement of XMT landslide; (b) horizontal displacement of XMT landslide; (c) vertical displacement of HJP landslide; (d) horizontal displacement of HJP landslide; (e) vertical deformation of LYY landslide; (f) horizontal displacement of LYY landslide. (P1, P2, and P3 correspond to the landslide investigation points in Section 3.2).

In conclusion, the two-dimensional displacement of landslides is positively correlated with rainfall, which is characterized by a higher deformation rate in the rainy season than in the non-rainy season and a significantly accelerated deformation process after concentrated rainfall. Rainfall is the main trigger factor of landslides in the Weining area. The positive correlation between rainfall and displacement acceleration is also reflected in the studies of the Jichang landslide and the Shibao landslide in the same geological conditions [49,50].

The primary sliding material is weathered basalt. Basalt itself often develops primary columnar joints. After weathering, basalts also have the characteristics of clay on the surface, including the cracking of shallow layers and the opening of weathered fissures [51]. The above factors provide the slope with a good channel for water intake. Under the action of rainfall, the pore water pressure of the landslide material increases and the strength of the geotechnical body decreases. In addition, rainwater enters the weak sliding surface along the cracks and joints, which reduces the shear strength of the sliding surface and intensifies the deformation of landslides [52].

### 5.2. Uncertainty Factors Affecting Landslide Classification

This paper proposes a remote sensing identification method for active landslide motion patterns based on geomorphic features as well as vertical and slope-oriented deformations. On this basis, the development characteristics and trigger factors of landslides in the Weining area are discussed by integrating geological conditions and daily precipitation data. However, the following limitations still exist in the research process.

First, InSAR technology can only identify slowly moving landslides. For landslides with fast movement in a short time, as their displacement exceeds the radar sensor's detection range, SAR image decorrelations will occur, resulting in the missed detection of landslides. The shadow and layover phenomena generated by radar observation result in the lack of a two-dimensional displacement in some areas, also affecting the accuracy of landslide motion pattern recognition.

Secondly, the surface displacement measured by InSAR may differ from the deep displacement of landslides. Although the motion-pattern-identification method proposed in this study established the connection between the two-dimensional kinematic characteristics and typical landslide patterns, it did not consider the influence of deep displacement on the kinematic patterns due to the lack of borehole data. In the following research, it is necessary to strengthen the study of slope structure characteristics to make the landslide deformation-pattern-recognition method proposed in this paper more applicable.

Finally, there are some errors in the two-dimensional decomposition displacement in the study area. In theory, the slope displacement is the combined displacement of north–south and east–west displacement values in the slope direction. Due to the satellite sensor not being sensitive to the north–south displacement, there are some errors in the slope displacement obtained. It is the systematic error of the satellite-based radar measurement. In addition, in the process of the displacement decomposition calculation, the landslide movement direction is inferred from the slope aspect, 3D terrain model and optical images. It may not be the exact sliding direction. The above two factors lead to some differences between the vertical and slope-oriented displacements and the real displacement. However, the obtained landslide displacement distribution characteristics and time-series displacement development trend are accurate, and it is effective to use these data to discuss the kinematic characteristics and influencing factors of landslides.

## 6. Conclusions

Catastrophic geological hazards frequently occur in southwest China due to the fragile geological environment, strong artificial activities, and precipitation. The early identification and classification of active landslide kinematic features are important for landslide prevention and management. This study proposes a remote sensing identification method for active landslide motion patterns by integrating geomorphic features as well as vertical and slope-oriented deformations. Among them, rotational landslides are characterized by similar vertical and horizontal deformation rates, with vertical deformation mainly occurring at the head and gradually decreasing along the slope, while horizontal deformation mainly occurs at the foot and gradually increases along the slope. As for the planar slide, the dominant deformation is in the horizontal direction. It is further classified into planar traction and planar thrust types according to the driving position. The vertical deformation of planar traction slides is concentrated at the foot, while the vertical deformation of planar thrust slides is concentrated at the head of the landslide.

Through the observation of multi-source radar images and two-dimensional displacement decomposition, we identified 21 active landslides in Weining, including 1 rotational landslide, 10 planar traction slides and 10 planar thrust slides. We verified the accuracy of the identification results through field geological surveys and UAV aerial photography. Integrating the daily rainfall and time-series displacement, we found that there was a significant positive correlation between landslide deformation acceleration and precipitation in the Weining area. The remote sensing identification method of active landslide movement patterns based on InSAR observations proposed in this paper can effectively detect the

kinematic characteristics and provide important support for geological disaster prevention and management.

**Author Contributions:** Conceptualization, Y.Z. and X.Y.; methodology, Y.Z.; software, X.Y.; validation, Y.Z., C.Y., Z.Z. and Z.G.; formal analysis, Y.Z., L.Y. and X.Y.; writing—original draft preparation, Y.Z. and X.Y.; writing—review and editing, X.Y. and Y.Z.; visualization, X.Y.; supervision, X.Y.; project administration, X.Y.; funding acquisition, X.Y. All authors have read and agreed to the published version of the manuscript.

**Funding:** This research was funded by the China Three Gorges Corporation YMJ(XLD)/(19)110, China Geology Survey Project (DD20221738-2), National Key R&D Program of China (2018YFC1505002) and National Science Foundation of China (41672359).

**Data Availability Statement:** SAR images are available at <https://scihub.copernicus.eu/dhus/#/Home> (accessed on 1 August 2020); Precipitation data are available at <https://cds.climate.copernicus.eu> (accessed on 1 August 2020).

**Acknowledgments:** We appreciate the editors and anonymous reviewers for their constructive comments, which were of great help in improving the manuscript.

**Conflicts of Interest:** The authors declare no conflict of interest.

## References

- Dai, F.C.; Xu, C.; Yao, X.; Xu, L.; Tu, X.B.; Gong, Q.M. Spatial distribution of landslides triggered by the 2008 Ms 8.0 Wenchuan earthquake, China. *J. Asian Earth Sci.* **2011**, *40*, 883–895. [[CrossRef](#)]
- Xu, C.; Xu, X.; Yao, X.; Dai, F. Three (nearly) complete inventories of landslides triggered by the May 12, 2008 Wenchuan Mw 7.9 earthquake of China and their spatial distribution statistical analysis. *Landslides* **2014**, *11*, 441–461. [[CrossRef](#)]
- Ju, Y.; Xu, Q.; Jin, S.; Li, W.; Su, Y.; Dong, X.; Guo, Q. Loess landslide detection using object detection algorithms in northwest China. *Remote Sens.* **2022**, *14*, 1182. [[CrossRef](#)]
- Rogers, A.E.E.; Ingalls, R.P. Venus: Mapping the surface reflectivity by radar interferometry. *Science* **1969**, *165*, 797–799. [[CrossRef](#)] [[PubMed](#)]
- Graham, L. Synthetic interferometer radar for topographic mapping. *Proc. IEEE* **1974**, *62*, 763–768. [[CrossRef](#)]
- Xu, Y.; Lu, Z.; Kim, J.-W. P-Band InSAR for geohazard detection over forested terrains: Preliminary results. *Remote Sens.* **2021**, *13*, 4575. [[CrossRef](#)]
- Wang, Y.; Liu, D.; Dong, J.; Zhang, L.; Guo, J.; Liao, M.; Gong, J. On the applicability of satellite SAR interferometry to landslide hazards detection in hilly areas: A case study of Shuicheng, Guizhou in southwest China. *Landslides* **2021**, *18*, 2609–2619. [[CrossRef](#)]
- Ren, K.; Yao, X.; Zhao, X.; Zhou, Z.; Li, L. Study of landslide failure prediction based on TS-InSAR, GPS and image offset monitoring. *Chin. J. Rock Mech. Eng.* **2020**, *39*, 3421–3431. [[CrossRef](#)]
- Sandwell, D.T.; Price, E.J. Phase gradient approach to stacking interferograms. *J. Geophys. Res.* **1998**, *103*, 30183–30204. [[CrossRef](#)]
- Ferretti, A.; Prati, C.; Rocca, F. Analysis of permanent scatterers in SAR interferometry. In Proceedings of the IGARSS 2000, IEEE 2000 International Geoscience and Remote Sensing Symposium. Taking the Pulse of the Planet: The Role of Remote Sensing in Managing the Environment, Honolulu, HI, USA, 24–28 July 2000; Volume 2, pp. 761–763.
- Berardino, P.; Fornaro, G.; Lanari, R.; Sansosti, E. A new algorithm for surface deformation monitoring based on small baseline differential SAR interferograms. *IEEE Trans. Geosci. Remote Sens.* **2002**, *40*, 2375–2383. [[CrossRef](#)]
- Liu, Y.; Yao, X.; Gu, Z.; Zhou, Z.; Liu, X.; Chen, X.; Wei, S. Study of the Automatic Recognition of Landslides by Using InSAR Images and the Improved Mask R-CNN Model in the Eastern Tibet Plateau. *Remote Sens.* **2022**, *14*, 3362. [[CrossRef](#)]
- Chen, X.; Yao, X.; Zhou, Z.; Liu, Y.; Yao, C.; Ren, K. DRs-UNet: A Deep Semantic Segmentation Network for the Recognition of Active Landslides from InSAR Imagery in the Three Rivers Region of the Qinghai–Tibet Plateau. *Remote Sens.* **2022**, *14*, 1848. [[CrossRef](#)]
- Zhu, Y.; Yao, X.; Yao, L.; Yao, C. Detection and characterization of active landslides with multisource SAR data and remote sensing in western Guizhou, China. *Nat. Hazards* **2022**, *111*, 973–994. [[CrossRef](#)]
- Li, L.; Yao, X.; Zhou, Z.; Wang, D. The applicability assessment of sentinel-1 data in InSAR monitoring of the deformed slopes of reservoir in the mountains of southwest China: A case study in the Xiluodu reservoir. *J. Geomech.* **2022**, *28*, 281–293. [[CrossRef](#)]
- Yao, C.; Yao, X.; Gu, Z.; Ren, K.; Zhou, Z. Analysis on the development law of active geological hazards in the loess plateau based on InSAR identification. *J. Geomech.* **2022**, *28*, 257–267. [[CrossRef](#)]
- Zhu, Y.; Yao, X.; Yao, L.; Zhou, Z. Identification and risk assessment of coal mining-induced landslides in Guizhou province by InSAR and optical remote sensing. *J. Geomech.* **2022**, *28*, 268–280. [[CrossRef](#)]
- Intrieri, E.; Raspini, F.; Fumagalli, A.; Lu, P.; Del Conte, S.; Farina, P.; Allievi, J.; Ferretti, A.; Casagli, N. The Maoxian landslide as seen from space: Detecting precursors of failure with sentinel-1 data. *Landslides* **2018**, *15*, 123–133. [[CrossRef](#)]

19. Reyes-Carmona, C.; Barra, A.; Galve, J.; Monserrat, O.; Pérez-Peña, J.; Mateos, R.; Notti, D.; Ruano, P.; Millares, A.; López-Vinielles, J.; et al. Sentinel-1 DInSAR for monitoring active landslides in critical infrastructures: The case of the rules reservoir (southern Spain). *Remote Sens.* **2020**, *12*, 809. [[CrossRef](#)]
20. Zhang, C.; Zhao, Y.; He, X.; Guo, J.; Yan, Y. Space-sky-surface integrated monitoring system for overburden migration regularity in shallow-buried high-intensity mining. *Bull. Eng. Geol. Environ.* **2021**, *80*, 1403–1417. [[CrossRef](#)]
21. Cascini, L.; Fornaro, G.; Peduto, D. Advanced low- and full-resolution DInSAR map generation for slow-moving landslide analysis at different scales. *Eng. Geol.* **2010**, *112*, 29–42. [[CrossRef](#)]
22. Bonforte, A.; Guglielmino, F.; Coltelli, M.; Ferretti, A.; Puglisi, G. Structural assessment of Mount Etna volcano from Permanent Scatterers analysis. *Geochem. Geophys. Geosyst.* **2011**, *12*. [[CrossRef](#)]
23. Li, T.; Motagh, M.; Wang, M.; Zhang, W.; Gong, C.; Xiong, X.; He, J.; Chen, L.; Liu, J. Earth and rock-filled dam monitoring by high-resolution X-band interferometry: Gongming dam case study. *Remote Sens.* **2019**, *11*, 246. [[CrossRef](#)]
24. Hu, J.; Li, Z.W.; Ding, X.L.; Zhu, J.J.; Zhang, L.; Sun, Q. Resolving three-dimensional surface displacements from InSAR measurements: A review. *Earth-Sci. Rev.* **2014**, *133*, 1–17. [[CrossRef](#)]
25. Ren, K.; Yao, X.; Li, R.; Zhou, Z.; Yao, C.; Jiang, S. 3D displacement and deformation mechanism of deep-seated gravitational slope deformation revealed by InSAR: A case study in Wudongde reservoir, Jinsha river. *Landslides* **2022**, *19*, 2159–2175. [[CrossRef](#)]
26. Yi, X.; Feng, W.; Wu, M.; Ye, Z.; Fang, Y.; Wang, P.; Li, R.; Dun, J. The initial impoundment of the Baihetan reservoir region (China) exacerbated the deformation of the Wangjiashan landslide: Characteristics and mechanism. *Landslides* **2022**, *19*, 1897–1912. [[CrossRef](#)]
27. Meng, Q.; Confuorto, P.; Peng, Y.; Raspini, F.; Bianchini, S.; Han, S.; Liu, H.; Casagli, N. Regional recognition and classification of active loess landslides using two-dimensional deformation derived from sentinel-1 interferometric radar data. *Remote Sens.* **2020**, *12*, 1541. [[CrossRef](#)]
28. Ali, J.R.; Thompson, G.M.; Zhou, M.-F.; Song, X. Emeishan large igneous province, SW China. *Lithos* **2005**, *79*, 475–489. [[CrossRef](#)]
29. He, K.; Ma, G.; Hu, X.; Luo, G.; Mei, X.; Liu, B.; He, X. Characteristics and mechanisms of coupled road and rainfall-induced landslide in Sichuan China. *Geomat. Nat. Hazards Risk* **2019**, *10*, 2313–2329. [[CrossRef](#)]
30. He, K.; Ma, G.; Hu, X. Formation mechanisms and evolution model of the tectonic-related ancient giant basalt landslide in Yanyuan county, China. *Nat. Hazards* **2021**, *106*, 2575–2597. [[CrossRef](#)]
31. Guo, J.; Yi, S.; Yin, Y.; Cui, Y.; Qin, M.; Li, T.; Wang, C. The effect of topography on landslide kinematics: A case study of the Jichang town landslide in Guizhou, China. *Landslides* **2020**, *17*, 959–973. [[CrossRef](#)]
32. Lanari, R.; Mora, O.; Manunta, M.; Mallorqui, J.J.; Berardino, P.; Sansosti, E. A small-baseline approach for investigating deformations on full-resolution differential SAR interferograms. *IEEE Trans. Geosci. Remote Sens.* **2004**, *42*, 1377–1386. [[CrossRef](#)]
33. Pepe, A.; Lanari, R. On the extension of the minimum cost flow algorithm for phase unwrapping of multitemporal differential SAR interferograms. *IEEE Trans. Geosci. Remote Sens.* **2006**, *44*, 2374–2383. [[CrossRef](#)]
34. Doin, M.-P.; Lasserre, C.; Peltzer, G.; Cavalié, O.; Doubre, C. Corrections of stratified tropospheric delays in SAR interferometry: Validation with global atmospheric models. *J. Appl. Geophys.* **2009**, *69*, 35–50. [[CrossRef](#)]
35. Morishita, Y.; Lazecky, M.; Wright, T.; Weiss, J.; Elliott, J.; Hooper, A. LiCSBAS: An open-source InSAR time series analysis package integrated with the LiCSAR automated sentinel-1 InSAR processor. *Remote Sens.* **2020**, *12*, 424. [[CrossRef](#)]
36. Zhu, Y.; Yao, X.; Yao, L.; Zhou, Z.; Ren, K.; Li, L.; Yao, C.; Gu, Z. Identifying the mechanism of toppling deformation by InSAR: A case study in Xiluodu reservoir, Jinsha river. *Landslides* **2022**, 1–17. [[CrossRef](#)]
37. Kang, Y. Application of InSAR Technology in Landslide Detection and Monitoring in Southwest Mountainous Area. Master's Thesis, Chang'an University, Xi'an, China, 2016.
38. Varnes, D.J. Landslide types and processes. *Landslides Eng. Pract.* **1958**, *24*, 20–47.
39. Hungr, O.; Leroueil, S.; Picarelli, L. The varnes classification of landslide types, an update. *Landslides* **2014**, *11*, 167–194. [[CrossRef](#)]
40. Xin, P.; Liu, Z.; Wu, S.; Liang, C.; Lin, C. Rotational–translational landslides in the Neogene basins at the northeast margin of the Tibetan plateau. *Eng. Geol.* **2018**, *244*, 107–115. [[CrossRef](#)]
41. Huang, H.; Song, K.; Yi, W.; Long, J.; Liu, Q.; Zhang, G. Use of multi-source remote sensing images to describe the sudden Shanshucao landslide in the three gorges reservoir, China. *Bull. Eng. Geol. Environ.* **2019**, *78*, 2591–2610. [[CrossRef](#)]
42. Li, D.; Yan, L.; Wu, L.; Yin, K.; Leo, C. The Hejiapingzi landslide in Weining county, Guizhou province, southwest China: A recent slow-moving landslide triggered by reservoir drawdown. *Landslides* **2019**, *16*, 1353–1365. [[CrossRef](#)]
43. Ma, S.; Xu, C.; Xu, X.; He, X.; Qian, H.; Jiao, Q.; Gao, W.; Yang, H.; Cui, Y.; Zhang, P.; et al. Characteristics and causes of the landslide on July 23, 2019 in Shuicheng, Guizhou province, China. *Landslides* **2020**, *17*, 1441–1452. [[CrossRef](#)]
44. Fan, X.; Tang, J.; Tian, S.; Jiang, Y. Rainfall-induced rapid and long-runout catastrophic landslide on July 23, 2019 in Shuicheng, Guizhou, China. *Landslides* **2020**, *17*, 2161–2171. [[CrossRef](#)]
45. Leng, Y.; Kong, X.; He, J.; Xing, A.; Zhang, Y.; Wang, Q. The July 10, 2020, Red-bed landslide triggered by continuous rainfall in Qianxi, Guizhou, China. *Landslides* **2022**, *19*, 1421–1433. [[CrossRef](#)]
46. Li, Y.; Feng, X.; Yao, A.; Zhang, Z.; Li, K.; Wang, Q.; Song, S. Progressive evolution and failure behavior of a Holocene river-damming landslide in the SE Tibetan plateau, China. *Landslides* **2022**, *19*, 1069–1086. [[CrossRef](#)]
47. Xin, P.; Dong, X.; Wu, S.; Shi, J. The accumulation characteristics and mechanism of rotational-translational landslides in the Neogene basins on the northeastern margin of Tibet plateau. *Acta Geol. Sin.* **2017**, *91*, 499–509.

48. He, K.; Hu, X.; Ma, G.; Liu, B. The reactivated mechanism of Boli village giant ancient basalt landslide in Yanyuan, Sichuan. *Rock Soil Mech.* **2020**, *41*, 3443–3455. [[CrossRef](#)]
49. Yu, H.; Li, C.; Zhou, J.-Q.; Gu, X.; Duan, Y.; Liao, L.; Chen, W.; Zhu, Y.; Long, J. A Large-scale obliquely inclined bedding rockslide triggered by heavy rainstorm on the 8th of July 2020 in Shibao village, Guizhou, China. *Landslides* **2022**, *19*, 1119–1130. [[CrossRef](#)]
50. Chen, Y.; He, X.; Xu, C.; Huang, Y.; Zhang, P.; Luo, Z.; Zhan, T. Development characteristics and causes of a fatal landslide occurred in Shuicheng, Guizhou province, China. *IJGI* **2022**, *11*, 119. [[CrossRef](#)]
51. Zheng, G.; Xu, Q.; Liu, X. The Jichang landslide on July 23, 2019 in Shuicheng, Guizhou: Characteristics and failure mechanism. *J. Eng. Geol.* **2020**, *28*, 541–556. [[CrossRef](#)]
52. Shen, Q.; Chen, X.; Wang, N. Analysis of mechanical parameters of slip surface for basalt landslide in Yunnan. *Rock Soil Mech.* **2006**, *27*, 2309–2313. [[CrossRef](#)]